Perturbation tuning of plasmon modes in semiconductor armchair nanoribbons

Mohsen Yarmohammadi*

Lehrstuhl für Theoretische Physik I, Technische Universität Dortmund, Otto-Hahn Straße 4, 44221 Dortmund, Germany and Department of Energy Engineering and Physics, Amirkabir University of Technology, 14588 Tehran, Iran

(Received 13 July 2018; revised manuscript received 5 September 2018; published 17 October 2018)

Motivated by recent demands of the nanoplasmonic community, quasi-one-dimensional nanoribbons have attracted significant attention as promising materials in logic applications. By using the linear response theory and the Green's function formulation, we demonstrate how external *local* perturbations affect both intra- and interband plasmons in semiconductor armchair nanoribbons (aNRs). To do so practically, we focus on the silicon carbide aNRs subjected to a test photon beam. Particularly, the interplay between intra- and interband charge-density excitations is compared by taking into account the impact of ribbon width, the electronic dopant, the Zeeman magnetic field, temperature, and the incident photon wave vector on the dielectric function qualitatively. Furthermore, the combined effect of both weak and strong perturbations is studied. We show that both the intraband and interband plasmon excitations have a high susceptibility to perturbations, leading to the different optical features of the system. Moreover, we found various perturbation-dependent threshold frequencies in which the undamped plasmon modes and plasmon resonances take place. Finally, the invalidity of the linear response theory at strong perturbations is discussed concisely. Generically, the propagation and confinement of plasmon modes in the presence of weak and strong perturbations are reported. Our findings are useful for experimentalists to tune the optical properties of low-dimensional materials by perturbations.

DOI: 10.1103/PhysRevB.98.155424

I. INTRODUCTION

Plasmons, the ubiquitous collective density oscillations of electrons, have recently attracted considerable attention both theoretically [1–8] and experimentally [9–16]. These oscillations can occur in metals, semimetals, and doped semiconductors [17,18] for many applications such as nanophotonics/photovoltaics [19–21] and sensing [22,23]. Plasmons in metals are mostly in the visible part of the electromagnetic spectrum [24], which limits the applications of the metal plasmons due to the lack of tunability of plasmon frequency and large plasmon loss proportional to small plasmon propagation length in the visible region [25].

Very recently, in the realm of low-dimensional materials, plasmons exhibit remarkable behaviors in contrast to the conventional crystalline solids [12,14,26–28]. For instance, it has been shown that the graphene [a two-dimensional (2D) layer of carbon atoms] plasmons are in the terahertz-to-midinfrared part [4,5,12,28–32], which make it tunable by a back gate [33–35]. On the other hand, the case of small propagation length can be solved by lowering the system dimensionality from 2D to quasi-one-dimensional (1D). From this point, graphene nanoribbons and related graphene-like nanoribbons are the proper candidates in the low-dimensional plasmonics. This is particularly true because of low plasmon propagation length found in nanoparticle plasmonic chains [36,37].

Obviously, the environment has a crucial role in 2D and quasi-1D plasmons due to the high sensitivity of wave-function propagation to the external perturbations which are able to change the wave-vector of host carriers. For example, the behaviors of plasmons in pristine graphene in the presence of impurity and phonons have been studied in Refs. [3,4,38–46]. They have reported that an incident photon with an ascertained wave-vector can excite a plasmon by scattering from charged impurities. Since the plasmon frequency is usually proportional to the electronic density of states in the long wavelength limit [47], the plasmon frequencies alter by changing the carrier concentration of the system. Electron induction using the external electronic dopant is also an electronic perturbation, which behaves like a defect.

In addition to the electronic perturbations, the magnetic perturbations can also affect the plasmon frequencies of the low-dimensional materials. Wu *et al.* [48] have calculated the dielectric function of graphene in a uniform perpendicular magnetic field. They have found that there is a critical wave-vector depending on the magnetic-field strength in which plasmon damping takes place. Furthermore, the effect of the external magnetic field on cobalt ferrite nanoparticles manifest itself in the refractive index [49]. In addition, the magneto-plasmons in graphene have been studied in numerous studies [48,50–52], which tell us that the energies of the unstable magneto-plasmons could be in the terahertz part of the electromagnetic spectrum. Also, in Ref. [53], the tunable plasmonic cloaks have been studied using the external magnetic field, leading to modification of the wavelength limit. Besides the numerous works on low-dimensional plasmonics in the presence of electronic perturbations, the study of plasmon frequencies in the presence of magnetic ones has remained elusive. Due to the low dimension of 2D and quasi-1D systems, the Zeeman magnetic field can couple

*mohsen.yarmohammadi@tu-dortmund.de

only to the spin degrees of freedom of electrons, leading to different distributions of carries. Actually, in the presence of Zeeman magnetic field, there is a phase mismatch between the incident wave vector of the electromagnetic field in free space and plasmons of the system, resulting in different plasmon frequencies.

Despite the intensive studies of the graphene plasmons, to the best of our knowledge, the semiconductor armchair nanoribbons (aNR) plasmons have not been studied well theoretically. Here, practically, we focus on the silicon carbide (SiC) aNRs. Like carbon (C), silicon (Si) also possesses a 2D honeycomb structure, so-called silicene, the silicon analog of graphene [54,55]. Despite the zero-band-gap characteristics of both graphene and silicene, the graphenelike SiC is a semiconductor with a finite band gap [56–60]. Furthermore, it has been reported that other SiC nanostructures can be made such as nanoribbons, nanotubes, and nanoflakes [61–66]. Although these efforts increase the motivation to realize 2D SiC, no truly 2D form of SiC has yet been realized to date. Actually, 2D-SiC monolayers can be viewed as composition tunable nanomaterials between the clean graphene and silicene.

We report a theoretical investigation of SiC aNR plasmons in the limit of low- and high-energy excitations in the presence of external local electronic and magnetic perturbations. The electronic perturbation in our model is characterized by the chemical potential induced by an electric field (for example), while the magnetic perturbation is a perpendicular Zeeman magnetic field, which couples to the electron spin only. Both perturbations locally induce an extra potential to the dynamics of carriers. In order to address the plasmon modes, in the present work, we use the linear response theory and the Green's function technique. We study SiC aNR plasmon excitations at different widths and temperatures in the presence of local perturbations mentioned above. We report that the plasmon modes can either propagate or be confined in the presence of weak and strong local perturbations.

This paper is organized as follows. In Sec. II, we use a 2D Dirac Hamiltonian model to analytically calculate the Green's functions. Consequently, the density-density response function is achieved in Sec. III. In Sec. IV, we explain the impact of width, chemical potential, the Zeeman magnetic field, temperature, and the incident wave vector of the electromagnetic field on SiC aNR plasmon modes. The combined effects of all these factors are studied in this section as well. Finally, we summarize our findings in Sec. V.

II. EFFECTIVE HAMILTONIAN MODE L AND GREEN'S FUNCTION

In order to describe our model, an infinite quasi-1D SiC aNR with the translational symmetry along the x direction is considered, as presented in Fig. 1. Since the zigzag nanoribbons present similar plasmonic features for our proof-of-principle study, we focus only on the armchair one [67]. In fact, since zigzag NRs are mostly in the semimetallic phase, tuning of the electronic phase in this family of NRs in order to study the electro-optical properties is less interesting for us. However, the optical properties of zigzag NRs have been investigated well in Ref. [68]. As for the chiral NRs, it has

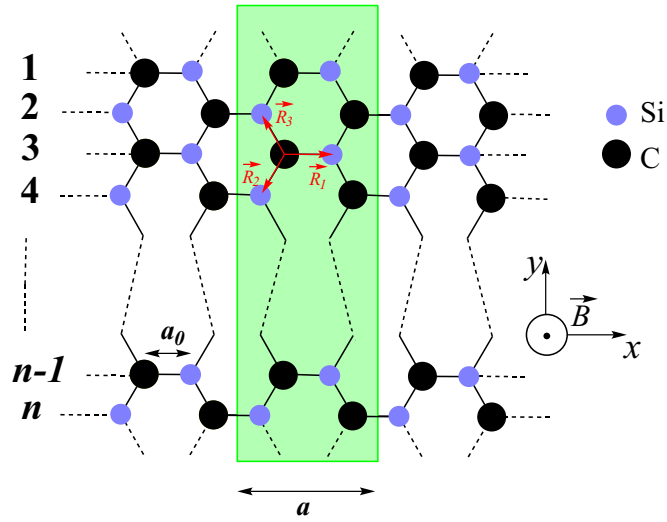

FIG. 1. The geometry of a SiC n-aNR. $a_0 \simeq 3.298$ Å denotes the interatomic distance between nearest-neighbor atoms [58]. The green box delimits the unit cells of the system and $a = 3a_0$ is the respective unit cell width. $\vec{R}_{\{1,2,3\}}$ are vectors corresponding to the nearest neighbors. Periodic boundary conditions are applied in the y direction. Additionally, the Zeeman magnetic field $\vec{B} = \mathcal{B}_z \hat{e}_z$ is applied to the system perpendicularly, shown by the symbol $\odot$.

been reported that the properties of this family are quite different than two other cases [69]. Our model is based on the tight-binding Hamiltonian including two interacting terms between the host electrons and the (i) electronic perturbation and (ii) magnetic perturbation. The former term refers to the on-site energies and external electronic dopant, whereas the latter is the external Zeeman magnetic field. It should be pointed out that the higher order hopping parameters can also be considered, leading to the electron-hole symmetry breaking in the electronic band structure and eventually different plasmonic properties. However, this is out of the scope of the present paper. For details, one can see Refs. [33,70]. The Hamiltonian models corresponding to these terms are given by

$$\hat{\mathcal{H}}_0 = \sum_{i,\sigma} \left[\varepsilon_0^{\mathrm{Si}} \hat{a}^\dagger_{i,\sigma} \hat{a}_{i,\sigma} + \varepsilon_0^{\mathrm{C}} \hat{b}^\dagger_{i,\sigma} \hat{b}_{i,\sigma}\right] - t \sum_{\langle i,j\rangle,\sigma} \hat{a}^\dagger_{i,\sigma} \hat{b}_{j,\sigma} - \mu \sum_{i,\sigma} [\hat{a}^\dagger_{i,\sigma} \hat{a}_{i,\sigma} + \hat{b}^\dagger_{i,\sigma} \hat{b}_{i,\sigma}] + \mathrm{H.c.}, \tag{1a}$$

$$\hat{\mathcal{H}}_Z = -g\mu_B \mathcal{B}_z/2 \sum_i [\hat{a}^\dagger_{i,\uparrow} \hat{a}_{i,\downarrow} + \hat{b}^\dagger_{i,\uparrow} \hat{b}_{i,\downarrow} + \mathrm{H.c.}], \tag{1b}$$

where the operator $\hat{c}_{i,\sigma}$ ($\hat{c}^\dagger_{i,\sigma}$) for $\hat{c} = \hat{a}$ is used to annihilate (create) an electron at the ith site of the lattice in the sublattice Si with spin σ and sublattice C for $\hat{c} = \hat{b}$. The coefficient $t = 1.42$ eV is the hopping parameter between nearest-neighbor atoms belonging to two sublattices Si and C and $\varepsilon_0^{\mathrm{Si}} = 0$ eV and $\varepsilon_0^{\mathrm{C}} = -2.85$ eV are the on-site energies of two different sublattice atoms, taken from Ref. [57]. Hereafter, we call sublattice Si and C as A and B, respectively. Furthermore, the quantity μ refers to the electronic dopant potential which is inducing an extra *on-site* potential to both sublattices isotropically. In the Zeeman term, the parameters g, μ_B, and $\mathcal{B}_z$ are

the degeneracy number, the Bohr magneton, and the strength of external magnetic field $\vec{B} = \mathcal{B}_z \hat{e}_z$, respectively. The term H.c. in both terms stands for the Hermitian conjugate. The Peierls phase factors stemming from the applied magnetic field which affects the band structure and the wave functions as quantum interferences manifest themselves in the hopping term $t_{n,m} = te^{2\pi \mathrm{i} \Delta\Phi_{n,m}}$. The details of derivation of $\Delta\Phi_{n,m}$ can be found in Appendix.

According to Fig. 1, each index site i contains the unit cell that can be labeled with index m and sublattices A_l and B_l for $l \in [1, n]$. After the Fourier transformation of annihilation and creation operators in Eqs. (1a) and (1b) into the momentum space, we expand them in terms of the basis sets $|A, k_x, k_y\rangle = \psi_A(k_x, k_y)$ and $|B, k_x, k_y\rangle = \psi_B(k_x, k_y)$ for sublattice A and B, respectively, in order to more easily handle the Hamiltonian and obtain the electronic spectrum of the system [71]. Thus, we use

$$\hat{c}^{\dagger}_{k_x,k_y} = \frac{1}{\sqrt{N_c}} \sum_{m=1}^{N_c} \sum_{l=1}^{n} e^{\mathrm{i}k_x x_m} \psi_c(l, k_y) \hat{c}^{\dagger}_{l,m}, \tag{2}$$

where x_m denotes the position of the mth unit cell along the x axis and $c = A$ and/or B. Also, $\hat{c}^{\dagger}_{l,m}$ creates an electron in the p_z orbit in the sublattice A/B with position l along the width of the ribbon (y axis) on the mth unit cell. In addition, in the prefactor, N_c is the number of unit cells. Following the work of Zheng *et al.* [71], the hard-wall boundary conditions lead to the wave functions for the y direction $\psi_c(l, k_y) = \sin(\sqrt{3}a_0 k_y l/2)$ with the discretized vertical wave vector $k_y = 2z\pi/(\sqrt{3}a_0[n+1])$, where $z = \{1, 2, 3, \ldots, n\}$. Rewriting the Hamiltonian in terms of operator $\hat{c}^{\dagger}_{k_x,k_y}$ defined in Eq. (2) results in the following band dispersion energy:

$$\mathcal{E}^{\sigma}_{\nu}(k_x, z) = \frac{\varepsilon_0^A + \varepsilon_0^B}{2} + \nu \sqrt{|\phi(k_x, z)|^2 + \left(\frac{\varepsilon_0^A - \varepsilon_0^B}{2}\right)^2} - \mu - \sigma h, \tag{3}$$

and the wave function made by operator $\hat{c}^{\dagger}_{k_x,z,\nu,\sigma}$,

$$\hat{c}^{\dagger}_{k_x,z,\nu,\sigma} = \frac{\sqrt{2}}{2}\left(\hat{a}^{\dagger}_{k_x,z,\sigma} + \nu \sqrt{\frac{\phi^*(k_x, z)}{\phi(k_x, z)}} \hat{b}^{\dagger}_{k_x,z,\sigma}\right). \tag{4}$$

In the equations above, the structure factor is defined by

$$\phi(k_x, z) := -\sum_{n,m} \sum_{\vec{k} \in \mathrm{FBZ}} t_{n,m} e^{-\mathrm{i}\vec{k}\cdot\vec{R}_{n,m}}, \tag{5}$$

where the momenta $\vec{k} = (k_x, k_y)$ belong to the first Brillouin zone (FBZ) of the SiC aNR structure.

Since a unit cell of aNRs includes $2n$ atoms, the Green's function in order to describe the particle-particle correlation can be written as a $2n \times 2n$ matrix. To this end, using the Matsubara formalism [72], each element of the Green's function matrix and the corresponding Fourier transformation can be described by

$$G^{\sigma}_{\alpha\beta}(t', k_x) = -\left\langle \mathcal{T}_{t'}\left[\hat{c}^{\sigma}_{k_x,\alpha}(t')\hat{c}^{\dagger,\sigma}_{k_x,\beta}(0)\right]\right\rangle,$$
$$G^{\sigma}_{\alpha\beta}(\mathrm{i}\omega_{\mathcal{F}}, k_x) = \int_0^{1/k_{\mathrm{B}}T} e^{\mathrm{i}\omega_{\mathcal{F}} t'} G^{\sigma}_{\alpha\beta}(t', k_x) dt', \tag{6}$$

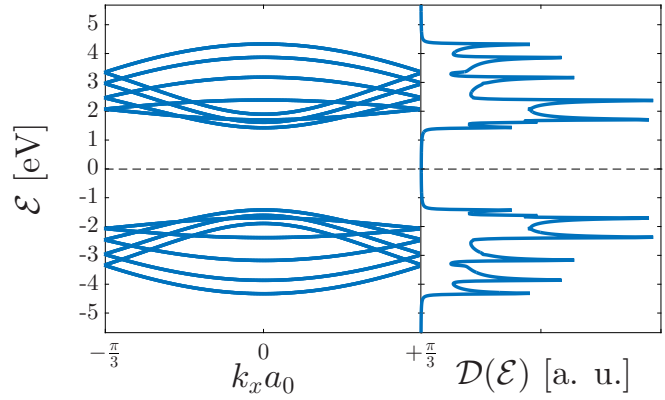

FIG. 2. The electronic band structure (left panel) and density of states (right panel) of SiC 8-aNR. The band gap is about 2.63 eV. In the electronic DOS panel, the van Hove singularities corresponding to the flat and almost flat bands, i.e., degenerate states, are evident. The dashed line is the Fermi level, which sets to the zero as the reference energy.

where α and β refer to each sublattice A and B, t' is the imaginary time, and $\mathcal{T}$ is the time-ordering operator. Also, the term $\omega_{\mathcal{F}} = (2\mathcal{F} + 1)\pi k_{\mathrm{B}} T$ is the fermionic Matsubara frequency (k_{B} is the Boltzman constant and T is the temperature). Therefore, elements $G^{\sigma}_{\alpha\beta}(\mathrm{i}\omega_{\mathcal{F}}, k_x)$ in the reciprocal space are calculated easily. Finally, by means of the Green's functions calculated above and tracing over the imaginary part of the Green's function, the electronic density of states (DOS) using the replacement $\mathrm{i}\omega_{\mathcal{F}} \to \mathcal{E} + \mathrm{i}0^+$ is given by

$$\mathcal{D}(\mathcal{E}) = -\frac{1}{\pi N_c} \sum_{\sigma,\alpha,k_x} \mathrm{Im}\left[G^{\sigma}_{\alpha\alpha}(\mathcal{E} + \mathrm{i}0^+, k_x)\right]. \tag{7}$$

Having the Green's function, the dynamical response function in order to study the plasmon modes in SiC aNR can be expressed. We will focus on this in the next section.

The distribution of electrons in SiC 8-aNR the electronic band structure (left panel) and DOS (right panel) in the absence of electronic and magnetic perturbations is shown in Fig. 2. The ribbon width $n = 8$ is chosen arbitrarily and there is no physical reason for this choice. This is only an example. This figure shows a 16-band structure with an electron-hole symmetry. The valance and conduction bands are macroscopically degenerate at several energy points, corresponding to the van Hove singularities (peaks) in the electronic DOS. As can be seen, SiC 8-aNR is a semiconductor system with the band gap about 2.63 eV for the width $n = 8$ in good agreement with Ref. [57] quantitatively. It should be noted that, generically, the band gap oscillates with n [57], leading to the ribbon width–dependent plasmon modes. In the next section, we use the Green's functions derived in Eq. (6) in order to study the dynamical response function of the system.

III. DYNAMICAL RESPONSE FUNCTION

In this section, we intend to calculate the response function of the system subjected to an applied photon beam. The polarization effects are activated by the photon with incident energy $\hbar\omega$ and the in-plane momenta $\mathbf{q} = (q_x, q_y)$. We start with the

density-density response function of noninteracting valence electrons in aNRs. Based on the linear response theory, the response function susceptibility $\chi^{(0)}$ is given by

$$\chi^{(0)}(\mathrm{i}\omega_p, q_x) = -\int_0^{1/k_\mathrm{B}T} dt' e^{\mathrm{i}\omega_p t'} \times \sum_\sigma \langle \mathcal{T}_{t'}[\hat{\rho}^\sigma(q_x, t')\hat{\rho}^\sigma(-q_x, 0)]\rangle, \quad (8)$$

wherein the charge density operator $\hat{\rho}^\sigma(q_x)$ is described by

$$\hat{\rho}^\sigma(q_x) = \frac{1}{N_c}\sum_{k_x,l}\left[\hat{c}^{\dagger,\sigma}_{A_l,k_x+q_x}\hat{c}^{\sigma}_{A_l,k_x} + \hat{c}^{\dagger,\sigma}_{B_l,k_x+q_x}\hat{c}^{\sigma}_{B_l,k_x}\right]. \quad (9)$$

Here, $\omega_p = 2p\pi k_\mathrm{B}T$ is the bosonic Matsubara frequency. To determine the density-density autocorrelation function inside the symbol $\langle\cdots\rangle$ in Eq. (8), we consider all correlation configurations using the Wick's theorem [72], which expresses the responses in terms of elements of noninteracting Green's functions obtained in Eq. (6) as

$$\chi^{(0)}_{\alpha\beta}(\mathrm{i}\omega_p, q_x) = \frac{k_\mathrm{B}T}{N_c}\sum_{k_x,\sigma,\mathcal{F}} G^\sigma_{\alpha\beta}(\mathrm{i}\omega_p + \mathrm{i}\omega_\mathcal{F}, k_x + q_x) \times G^\sigma_{\beta\alpha}(\mathrm{i}\omega_\mathcal{F}, k_x), \quad (10)$$

Finally, after pretty simple calculations, the expression for dynamical susceptibility can be obtained. In numerical calculations, as usual, the terms dealing with the fermionic and bosonic Matsubara frequencies are approximated with

$$\mathrm{i}\omega_\mathcal{F} := \mathcal{E} + \mathrm{i}0^+, \quad (11a)$$

$$\mathrm{i}\omega_p := \omega + \mathrm{i}0^+, \quad (11b)$$

where $-4\ \mathrm{eV} \leqslant \mathcal{E} \leqslant +4\ \mathrm{eV}$, $0\ \mathrm{eV} \leqslant \hbar\omega \leqslant 8\ \mathrm{eV}$, and $0^+ = 10\ \mathrm{meV}$ is the broadening factor. This value of 0^+ is chosen because the curves have sharper peaks, otherwise, a range of values larger than 10 meV gives the same results but with more broadened peaks, which is not convenient for the analysis. It is clear that the response function $\chi^{(0)}(\omega, q_x)$ has two real and imaginary parts, namely, $\chi^{(0)}_1(\omega, q_x)$ and $\chi^{(0)}_2(\omega, q_x)$, respectively. It implies that one can write

$$\chi^{(0)}(\omega, q_x) = \chi^{(0)}_1(\omega, q_x) + \mathrm{i}\chi^{(0)}_2(\omega, q_x). \quad (12)$$

Given the complex dynamical susceptibility or dielectric function $\chi^{(0)}(\omega, q_x)$, all optical properties of the system such as reflectivity, refractive index, and the absorption spectrum can be obtained. It is necessary to give a brief physical meaning of these real and imaginary parts. Generically, while the real part $\chi^{(0)}_1(\omega, q_x)$ refers to the refractive index, the imaginary part $\chi^{(0)}_2(\omega, q_x)$ describes the transition between the occupied valence bands and the unoccupied conduction bands. From these parts, we get various spectra information, which stems from the microcosmic physical process between the intra- and interband transition and solid electronic structure. For instance, the zeros of the real part correspond to the plasmon excitation frequencies. The nonzeros of the imaginary part give the well-known Landau damping and if both happen simultaneously, the plasmon resonances emerge. The Landau damping is of high importance in modern plasmonics

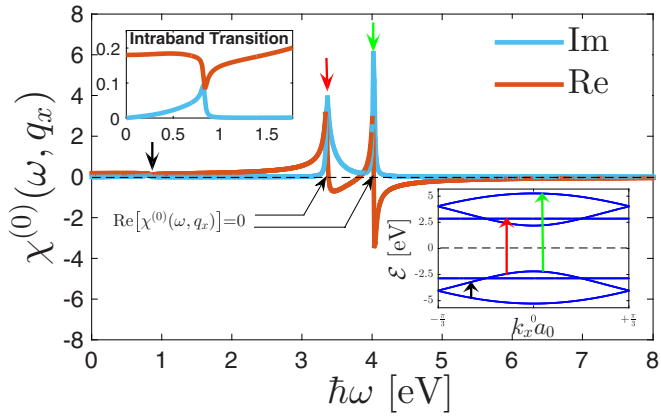

FIG. 3. Response function as a function of photon energy $\hbar\omega$ for *undoped* semiconductor SiC 3-aNR in the *absence* of Zeeman magnetic field. The thermal energy is set to $k_\mathrm{B}T = 0.35$ eV. The intraband transition is shown in top left inset panel. The peaks of the imaginary part and the zeros of the real part are labeled by arrows. Also, the electronic band structure of SiC 3-aNR is presented in bottom right inset panel, which tells us where the peaks come from. The incident wave vector is set to $|q_x a_0| = \pi/6$.

originating from the aim of miniaturization [73,74]. Furthermore, an undamped plasmon mode occurs at a frequency when both parts are zero. In the following, we will focus on these features.

The imaginary and real parts of the response function $\chi^{(0)}(\omega, q_x)$ in the case SiC 3-aNR at temperature $k_\mathrm{B}T = 0.35$ eV, the chemical potential $\mu = 0$ eV, and in the absence of Zeeman magnetic field are presented in Fig. 3. The wave vector of the incident photon is set to $|q_x a_0| = \pi/6$. The ribbon width $n = 3$ and also incident photon wave vector $|q_x a_0| = \pi/6$ are chosen for simplicity first in order to have nonmessy curves and there is no physical reason behind these choices. In Fig. 3, curves of both parts can be divided into three regions: (i) from 0 to 1 eV corresponding to the *infrared rays*, (ii) from 1 to 3 eV corresponding to the combined *infrared rays* and *visible light*, and (iii) from 3 to 8 eV corresponding to the combined *visible–ultraviolet light* regions of the electromagnetic spectrum. As mentioned, the constant peaks of both parts are described by the electronic band structure and DOS. Below the photon energy of about 2.63 eV corresponding to the band gap of the system, the imaginary part is zero except at the point $\hbar\omega \simeq 0.8$ eV, which is interestingly nonzero and shows an *intraband* transition in the valence bands (see the top left inset panel). Indeed, this intraband transition originates from the role of temperature from which the induced collision to electrons will result in the excitation of electrons in the valence bands. In turn, the photon excites electron/hole between valence bands because of this collision. All the higher peaks corresponding to *interband* transitions take place at the photon energies above the photon energy $\hbar\omega \simeq 2.63$ eV.

It is worthwhile to mention that all features described, i.e., the plasmon modes (when $\mathrm{Re}[\chi^{(0)}(\omega, q_x)] = 0$), the plasmon resonances (when $\mathrm{Re}[\chi^{(0)}(\omega, q_x)] = 0$ and $\mathrm{Im}[\chi^{(0)}(\omega, q_x)] \neq 0$ simultaneously), and the Landau damping (when $\mathrm{Im}[\chi^{(0)}(\omega, q_x)] \neq 0$) manifest themselves in the

interband regime. At higher incident energies, i.e., $\hbar\omega \geqslant 6$ eV, the electronic transition between the bands does not occur and the system is optically transparent. As for the refractive index, it should be noted that the maximum refraction occurs at lower frequencies and the propagation orientation of the electrons in the system is reversed at 3.25 eV $< \hbar\omega <$ 4 eV and $\hbar\omega >$ 4 eV due to the negative values of the real part.

In what follows, we show the numerical results for dynamical susceptibility in order to treat the impact of perturbations on the features mentioned above in SiC aNRs. In other words, we investigate the dielectric function of the system in the presence of external local perturbation whether electronic or magnetic in a more widespread scheme.

IV. RESULTS AND DISCUSSIONS

This section is divided into six parts. First, the response function of the different widths of SiC aNR is obtained. Second, the effect of an electronic dopant on both the imaginary and real parts of $\chi^{(0)}(\omega, q_x)$ is investigated. Third, we calculate the Zeeman magnetic-field effects on the transitions between bands and the refractive index. Fourth, the temperature evolution of the plasmon modes is studied. Fifth, we study the effect of the incident photon wave vector on $\chi^{(0)}(\omega, q_x)$ and finally, the combined effects of weak and strong factors above are explored simultaneously. In fact, we evaluate several extrinsic perturbations associated with the host electrons in order to see the charge excitations in aNRs. It should be noted that the results are valid for other semiconductor aNRs such as graphene aNRs, boron-nitride aNRs, beryllium monoxide aNRs, etc. Also, since the dispersion energy relation frequency ω versus the wave vector $\mathbf{q}$ has been studied in many works, we ignore the information of this feature in the present work. In addition to this property, the corresponding energy-loss function $L(\omega, q_x) = \mathrm{Im}[\chi^{(0)}(\omega, q_x)]^{-1}$ can be calculated, too. However, in the present paper, the main features of the optical properties are given by the imaginary and real parts of $\chi^{(0)}(\omega, q_x)$ only and we will not confuse the reader with many plots. For this reason, we neglect $L(\omega, q_x)$ plots. We stress that unless otherwise stated explicitly, the constants $\hbar = k_B = g = \mu_B = e = m_e = 1$ are used throughout the paper in numerical calculations for simplicity. Further, the interatomic distance is also set to 1, i.e., $a_0 = 1$ m. By this, one can determine the values of quantities q_x, ω, and T in their main units such as Å^{-1}, Hz, and Kelvin.

In our numerical calculations, we have picked ultranarrow widths only to make sure the band gap of the system is high enough in order to separate the behaviors of the intra- and interband transitions more precisely [75]. On the other hand, it has been shown that the ultranarrow aNRs have more remarkable optical properties than their 2D forms [76]. These are the reasons for our choices.

A. Ribbon width effects

In Fig. 4, we demonstrate how the ribbon width affects the dielectric function of *undoped* SiC n-aNR when the magnetic field is *absent*. The temperature and the photon wave vector are set to $k_B T = 0.35$ eV and $|q_x a_0| = \pi/6$, respectively. Figure 4(a) shows that at low frequencies around $\hbar\omega = 1$ eV,

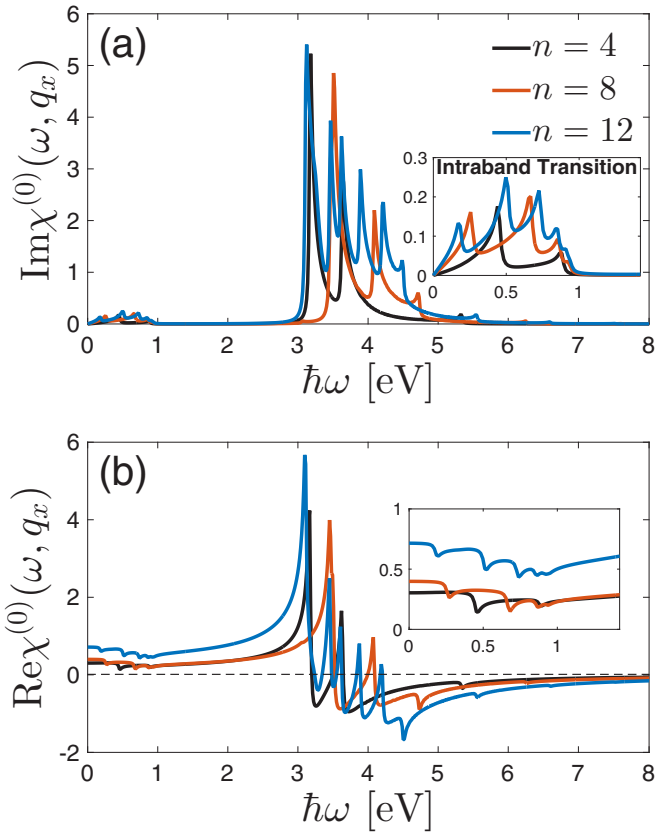

FIG. 4. The imaginary (a) and real (b) parts of the response function $\chi^{(0)}(\omega, q_x)$ for different ribbon widths when the temperature, the chemical potential, and the Zeeman magnetic field are fixed at $k_B T = 0.35$ eV, $\mu = 0$ eV, and $g\mu_B \mathcal{B}_z = 0$ eV, respectively. The incident photon wave vector is set to $|q_x a_0| = \pi/6$. The inset panels correspond to the low-frequency transitions and propagations in (a) and (b), respectively. The changes of both intraband and interband modes are clear when the ribbon width is altered.

there is no plasmon resonance for intraband transitions (corresponding to the visible light region of the electromagnetic spectrum) because there is no zero crossing in the real part in this range [see panel (b)]. Further, the number of intraband transitions increases when the ribbon width is increased. This can be understood from the fact that the number of bands in the electronic band structure depends strongly on the ribbon width [77,78]. Also, one can see that there is no Landau damping plasmon mode in the range 1 eV $< \hbar\omega <$ 3 eV due to the zero value of the imaginary part in this range. On the other hand, for interband transitions ($\hbar\omega >$ 3 eV), plasmon resonances show that the frequency of plasmons depends on the ribbon width and does not have a trend in good order. For instance, the first resonance for $n = 4$ appears at $\hbar\omega =$ 3.25 eV, while for $n = 8$, it takes place at $\hbar\omega = 3.5$ eV. And finally for $n = 12$, it emerges at $\hbar\omega = 3$ eV. Therefore, interband plasmon modes oscillate with ribbon width, which refers to the oscillatory dependence of the band gap to the ribbon width [78]. However, the Landau undamping region does not depend on the ribbon width and it is from 1 to 3 eV (between intraband and interband transitions) always. In fact, we conclude that the interplay of the intraband and interband

plasmons can be controlled by the ribbon width. At higher frequencies, there is no transition and the system is optically transparent; the intensity of this transparency depends on the ribbon width.

As for the real part, one finds corresponding modifications when the ribbon width is increased. At energies below the threshold $\hbar\omega = 3$ eV, the real part increases with n, which reflects the increase in the number of charge carriers. Furthermore, the modes below this threshold are well resolved in energy, leading to nonzero values of the real part and no reversion in the propagation of the electrons. Above this point, interband plasmon excitations proportional to the ribbon width make the real part of $\chi^{(0)}(\omega, q_x)$ cross the zero axis several times depending on n. Finally, after $\hbar\omega = 4.25$ eV, the propagation of the electrons is completely reversed independent of the ribbon width.

B. Electronic dopant effects

For the case of extrinsic doping from an electronic dopant, characterized by the chemical potential μ, the numerical data of the dielectric function of SiC 10-aNR for nonzero doping μ, namely, $\mu = 0$, 0.3, 1.2, 2.2, and 4.25 eV at $k_BT = 0.35$ eV, $|q_x a_0| = \pi/6$, and $g\mu_B\mathcal{B}_z = 0$ eV are reported in Fig. 5. Figure 5(a) indicates the behavior of the imaginary part of $\chi^{(0)}(\omega, q_x)$ as a function of frequency $\hbar\omega$ when the doping level is increased from zero to 4.25 eV. We have expanded the energy range of doping here in addition to other reported works [79,80]. From the panel (a), one finds an exotic behavior for $\chi^{(0)}(\omega, q_x)$ (both parts) at strong $\mu = 4.25$ eV because the number of intraband modes decreases suddenly to one and there is no interband mode at $\hbar\omega \geqslant 1$ eV. This refers to the invalidity of the linear response theory at this strong perturbation. It is clear that the appeared intraband mode will take place at zero as the chemical potential is increased further, i.e., more than 4.25 eV. Interestingly, at small doping levels, i.e., $\mu < 2$ eV, the dielectric function is not enhanced significantly because the number of charge carriers is still not high enough to affect the dispersion frequencies. Furthermore, in addition to the explanation provided on the lack of the Landau damping in the range of 1 eV $< \omega/t <$ 3 eV, one can observe that the plasmon intraband modes have a high susceptibility to μ, whereas the interband ones are not affected much. Given the invalidity of the linear response theory at $\mu = 4.25$ eV, transparency property for $\hbar\omega \geqslant 3$ eV cannot be concluded for this high μ.

Our findings also demonstrate an unusual treatment mentioned above for the refractive index at $\mu > 2.2$ eV. In contrast to the effect of ribbon width, the real part of the dielectric function shows a reversed propagation orientation of electrons even at low frequencies when the doping level is increased. These results are not found in the case of 2D systems. For instance, in Ref. [80], the authors have reported that both real and imaginary parts of the dielectric function alter with doping level even at lower values than the hopping energy t, while this is not the case in quasi-1D aNRs, as presented above. While the plasmon resonance modes appear at very high frequencies several times, unlike the ribbon width effect, it occurs even at the frequency $\hbar\omega \leqslant 1$ eV. Finally, it should be pointed out that the system is not optically transparent in the presence of an electronic dopant for the photon energy range of 0–8 eV.

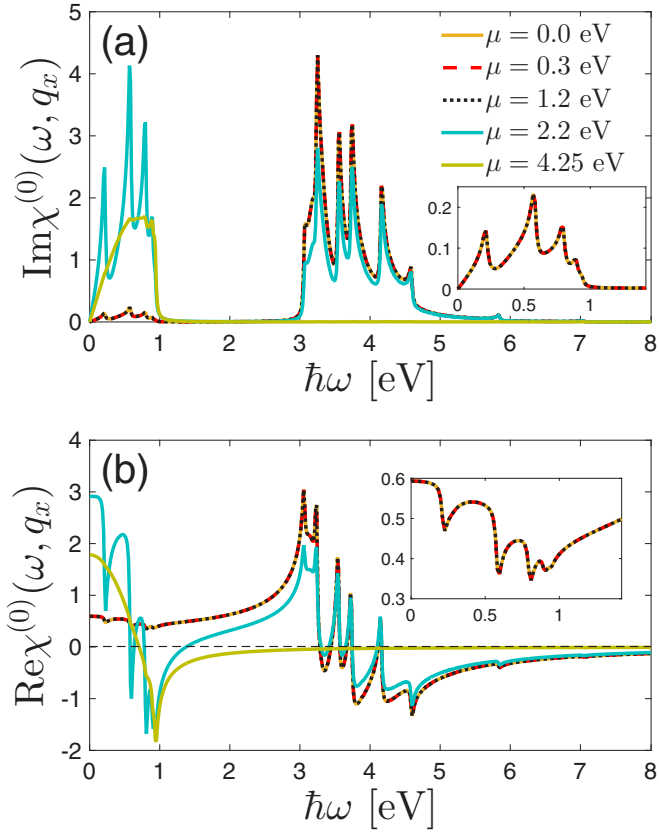

FIG. 5. The imaginary (a) and real (b) parts of the frequency-dependent dielectric function when the electronic dopant is doped. Emergence of the quasi-1D plasmon upon increasing the doping level is evident. Further, one finds different behaviors of intraband and interband modes in the curves. The quantities $k_BT = 0.35$ eV, $|q_x a_0| = \pi/6$, $g\mu_B\mathcal{B}_z = 0$ eV, and $n = 10$ are considered in these plots. The inset panels in (a) and (b) refer to the low-energy excitations and refractivity of the system, respectively.

C. Zeeman magnetic-field effects

The frequency-dependent dielectric function $\chi^{(0)}(\omega, q_x)$ of SiC 10-aNR as a function of the Zeeman magnetic field is displayed in Fig. 6. The magnetic field varies from 0 to 4.25 eV at thermal voltage $k_BT = 0.35$ eV, the zero doping level $\mu = 0$ eV, and $|q_x a_0| = \pi/6$. In strong contrast to the case of doping, in which at low frequencies, intraband plasmons are not changed with low doping levels, the intraband plasmons in this case (various magnetic fields) change with even weak strengths of the magnetic field, as shown in Fig. 6(a). In other words, the imaginary part increases slightly with the magnetic field up to $g\mu_B\mathcal{B}_z = 2.2$ eV and after that, it starts to decrease, leading to one intraband charge excitation only and no interband transition, stemming from the invalidity of the linear response theory at strong magnetic-field strengths. Upon increasing the magnetic field, the scattering rate of carriers in the system is also increased because, for an ascertained energy of carriers, the carriers get an extra potential by the magnetic field. This implies

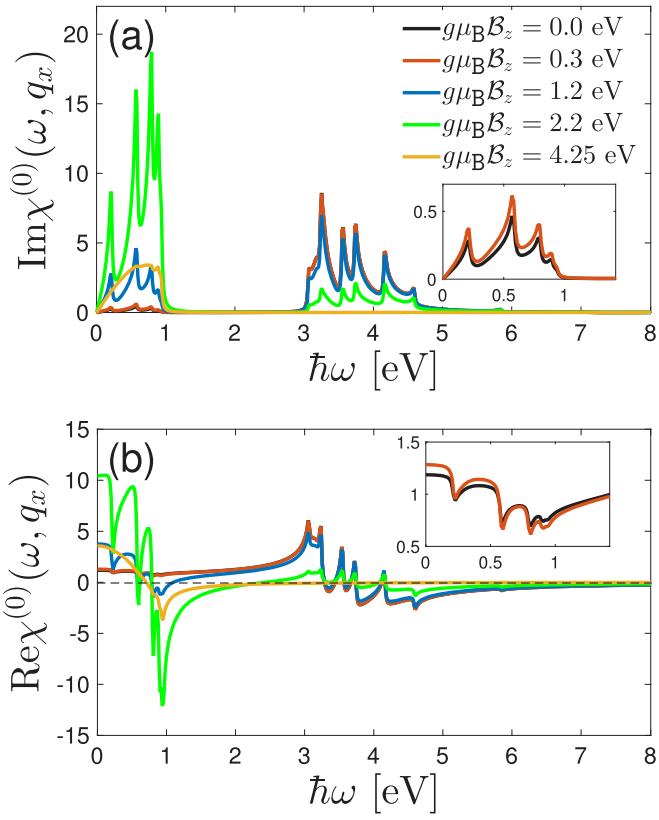

FIG. 6. Calculated frequency-dependent (a) imaginary and (b) real parts of the dielectric function of SiC 10-aNR when various magnetic-field strengths are applied at $k_BT = 0.35$ eV, $|q_xa_0| = \pi/6$, and $\mu = 0$ eV. Further, the changes of low-frequency limits of both imaginary and real parts are magnified in the inset panels.

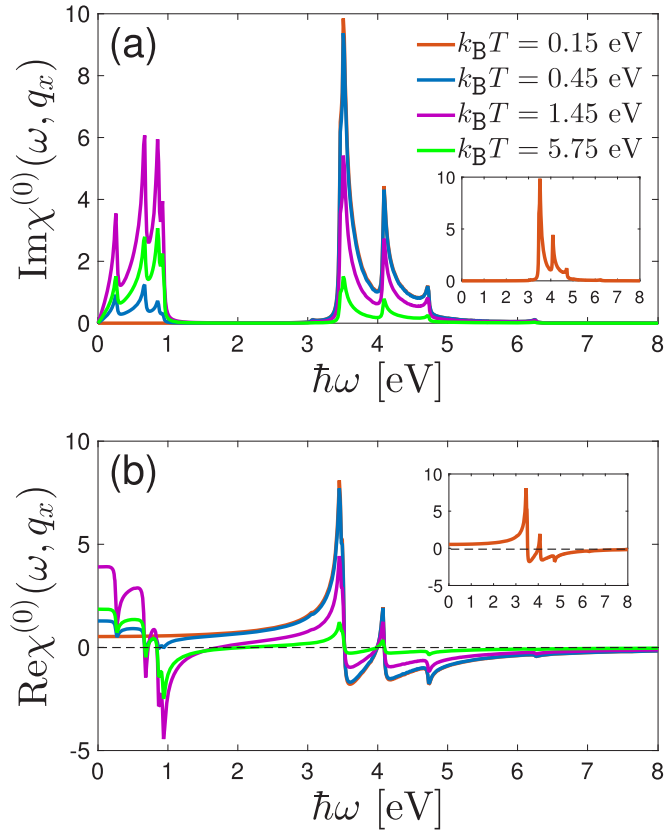

FIG. 7. The frequency dependence of the (a) imaginary and (b) real parts of $\chi^{(0)}(\omega, q_x)$ of SiC 10-aNR as a function of temperature at $g\mu_B\mathcal{B}_z = 0$ eV, $|q_xa_0| = \pi/6$, and $\mu = 0$ eV. The inset panels show the $k_BT = 0.15$ eV case for imaginary and real parts in (a) and (b), respectively. It can be seen that there is no intraband transition and optical feature at fairly low temperatures.

that the scattering processes of the carriers change due to the Zeeman magnetic-field-induced potential. As seen, contrary to the intraband transitions, the interband ones decrease with the magnetic field. Also, the Landau undamping occurs again in the range of 1 eV $< \hbar\omega <$ 3 eV and $\hbar\omega >$ 6 eV for the weak magnetic fields, i.e., $g\mu_B\mathcal{B}_z <$ 4.25 eV. Similar to the case of the electronic dopant, plasmon resonances emerge for both intra- and interband modes.

In Fig. 6(b) we present the real part of the dielectric function at finite temperature $k_BT = 0.35$ eV and various magnetic fields. The real part crosses the zero axis for weak magnetic fields to showcase the reversion of the propagation direction of the carriers corresponding to the plasmon excitations frequencies. Nevertheless, contrary to the case of μ for which there is no transparency for the system optically, the system in the presence of the magnetic fields $g\mu_B\mathcal{B}_z <$ 4.25 eV is optically transparent for $\hbar\omega \geqslant 6.5$ eV.

D. Temperature effects

In order to study the effect of temperature on the dielectric function of SiC aNRs, we present in Fig. 7 the imaginary and real parts of frequency-dependent $\chi^{(0)}(\omega, q_x)$ at $g\mu_B\mathcal{B}_z = 0$ eV, $|q_xa_0| = \pi/6$, $n = 10$, and $\mu = 0$ eV for various temperatures when dealing with the intra- and interband transitions and the corresponding refractions. At fairly low temperatures, i.e., $k_BT = 0.15$ eV, the imaginary part of $\chi^{(0)}(\omega, q_x)$ is zero at frequencies below the threshold $\hbar\omega =$ 3 eV. In this region, there is no intraband plasmon mode because there is no peak [see the inset panel in (a)]. One only observes the interband transitions at energies above this threshold. Upon the increase in temperature, the intraband plasmon modes (low-energy side) show up and the height of modes increases when the temperature is increased further up to $k_BT = 1.45$ eV. This refers to the increase in the collision process of charge carriers when the temperature is raised. Interestingly enough, one can see that the interband transitions decrease gradually with no threshold for the thermal energy. This is related to the temperature-dependent susceptibility, which tells us there is a critical temperature in which the static response function increases (decreases) with T before (after) that [77,81]. These results are in agreement with Ref. [80] qualitatively.

A similar interplay in comparison with the case of doping and the magnetic field at low and high intensities is observed for the real part in Fig. 7(b) when the temperature is increased. We see that the zeros of the real part of $\chi^{(0)}(\omega, q_x)$ correspond precisely to the frequencies when the imaginary part possesses peaks, resulting in plasmon resonances. In this case, the direction of the wave vector of electrons reverses again at

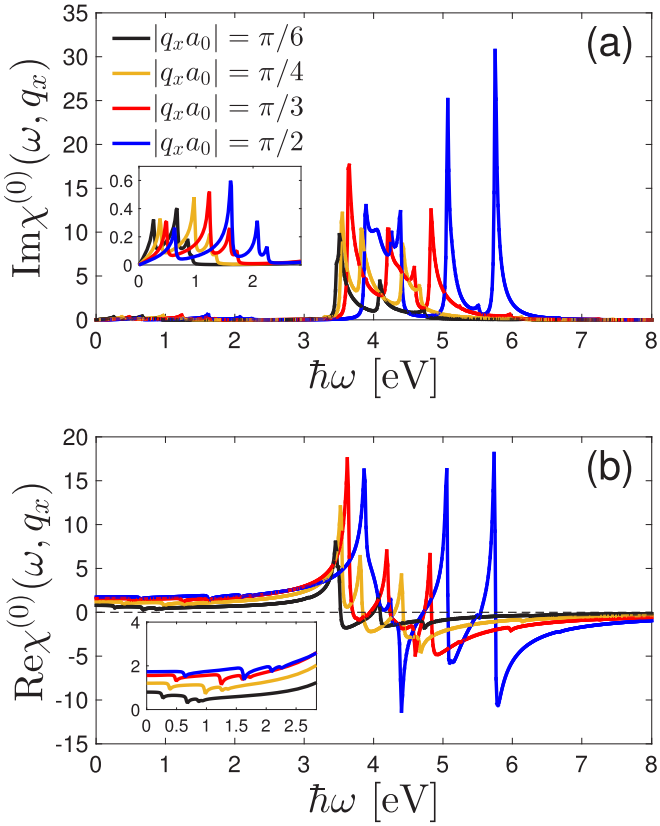

FIG. 8. The effect of the incident photon wave vector on the (a) imaginary and (b) real parts of the dielectric function $\chi^{(0)}(\omega, q_x)$ of SiC 10-aNR in the absence of both electronic and magnetic perturbations at $k_B T = 0.35$ eV. The inset panels clarify the behaviors of the low-energy regime, which give rise to fascinating changes when $|q_x a_0|$ is changed.

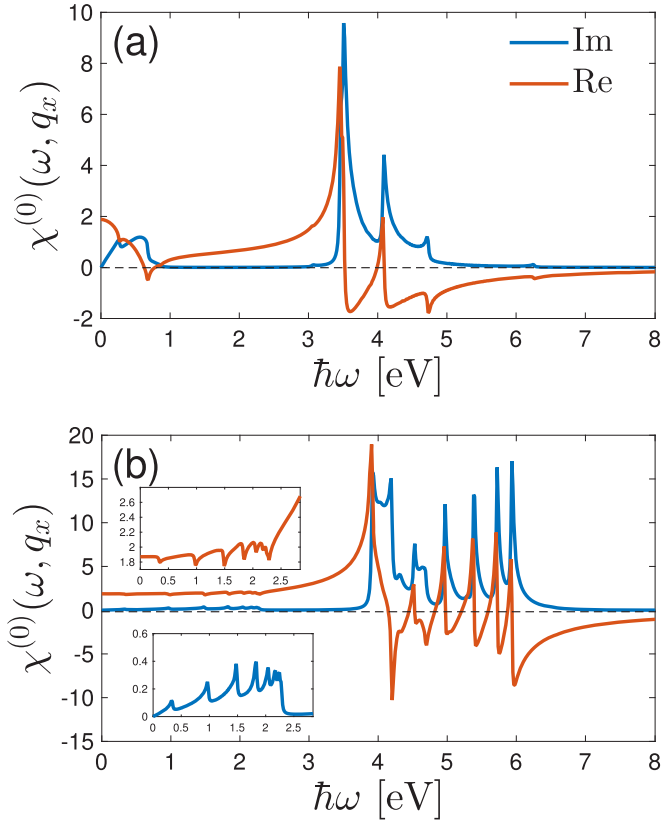

FIG. 9. Combined effects of electronic and magnetic perturbations on the dielectric function $\chi^{(0)}(\omega, q_x)$ at (a) $k_B T = 0.7$ eV, $\mu = 0.7$ eV, $g\mu_B \mathcal{B}_z = 0.7$ eV, and $|q_x a_0| = \pi/3$, and (b) $k_B T = 1.45$ eV, $\mu = 2.2$ eV, $g\mu_B \mathcal{B}_z = 2.2$ eV, and $|q_x a_0| = \pi/2$. No plasmon resonance at the low-energy side is presented in the inset panels of (b).

$\hbar\omega > 4$ eV, while the sign of the wave vector becomes positive and negative several times in the low-energy side $\hbar\omega < 4$ eV. Contrary to the previous cases, the undamped plasmon modes appear only at $\hbar\omega > 5.5$ eV for high temperatures and for low temperatures ($k_B T < 1$ eV), it happens at very high frequencies out of the considered range 0–8 eV.

E. Incident wave vector of test photon effects

Up to now, we used a fixed incident wave vector of the test photon. However, it can be changed, affecting the optical properties of the system. Let us compare the imaginary and real parts of $\chi^{(0)}(\omega, q_x)$ for the case of $|q_x a_0| \in [\pi/6 - \pi/2]$ when there is no perturbation, either electronic or magnetic at temperature $k_B T = 0.35$ eV. For the case of closely parallel to the SiC sheet, i.e., $|q_x a_0| = \pi/6$, the Landau undamping occurs at 1 eV $< \hbar\omega <$ 3 eV and $\hbar\omega >$ 5 eV, as presented in Fig. 8(a). However, for larger angles of the incident wave vector, i.e., $\pi/6 < |q_x a_0| \leqslant \pi/2$, these regions for the Landau undamping shift toward the higher frequencies and one can find the relation $\omega \propto \sqrt{|q_x|}$ in agreement with Ref. [80] qualitatively. This means that both intraband and interband charge excitations depend strongly on the incident wave vector of the test photon applied to the system. On the other hand, the height of the peaks corresponding to plasmon excitation frequencies increases when the wave vector $|q_x a_0|$ is increased further. Actually, it refers to the scattering process of carriers when they interact with photons with different incident angles. This affects the refraction property as well, as illustrated in Fig. 8(b). The refractive index gets zero value at higher frequencies as soon as $|q_x a_0|$ becomes closer to the perpendicular angle. Furthermore, there is no plasmon intraband resonance because, in the real part, there is no zero crossing. As for the undamped plasmon modes, as a result, the corresponding frequencies increase with the wave vector and for the perpendicular case, i.e., $|q_x a_0| = \pi/2$, there is no damping mode in the frequency energy range 0–8 eV.

F. Combined effects of electronic and magnetic perturbations

In the last paragraph of this section, we elaborate on the combined effects of both weak and strong perturbations on the dielectric function. To this end, we first consider a SiC 8-aNR at the temperature $k_B T = 0.7$ eV, the chemical potential $\mu = 0.7$ eV, and the magnetic field $g\mu_B \mathcal{B}_z = 0.7$ eV when the photon wave vector is $|q_x a_0| = \pi/3$, as illustrated in Fig. 9(a). Then, strong perturbations are considered in Fig. 9(b) with values $k_B T = 1.45$ eV, $\mu = 2.2$ eV, and $g\mu_B \mathcal{B}_z = 2.2$ eV at $|q_x a_0| = \pi/2$. At first glance, one observes an intraband plasmon resonance mode around the energy $\hbar\omega \simeq 0.8$ eV in

which the imaginary part gets the peak while the real part crosses the zero axis at the same time. On the other hand, more than one resonance appears for the interband plasmon modes at $\hbar\omega > 3$ eV. The number of intra- and interband transitions are not much in the case of $n = 8$ [Fig. 9(a)]. Furthermore, the Landau undamping emerges in the range of $\hbar\omega = [1 - 3]$ eV and $\hbar\omega > 6.25$ eV. The curves for $\hbar\omega \geqslant 7.5$ eV tell us that both real and imaginary parts get zero values, which means that the system is optically transparent.

From panel (b), one finds more transitions in both low-energy and high-energy regimes in the case of $n = 16$. It can be seen that there is no plasmon resonance for the intraband transitions because the real part does not cross any point and only the system deals with the interband plasmon resonances. Also, compared to $n = 8$, the Landau undamping takes place within a narrower region ($\hbar\omega = [2.5–3.25]$ eV). In addition, transparency cannot occur within the range of photon energy 0–8 eV when strong perturbations and a wider width of aNR are considered.

V. CONCLUSIONS

We have investigated theoretically the charge response of quasi-1D aNRs (SiC in our case) to external local electronic and magnetic perturbations based on the Green's function approach, followed by the linear response theory. All the studied responses are characterized by two energy regions, one below the band gap energy of about 2.63 eV and another one above the band gap corresponding to intraband and interband plasmon modes, respectively. We found that both the intraband and interband modes are strongly sensitive to geometrical parameters and also the extrinsic perturbations. In addition, we have explained the plasmonic properties of aNRs when a temperature gradient is applied. Furthermore, the plasmonic properties are studied in the presence of the combined effects of weak and strong perturbations for different ribbon widths. The important outcome is significant deviations for dielectric function when the perturbations are combined and/or not, leading to the different optical transparency of aNRs. Also, we have studied the refractive index to explore the propagation direction of host charges when applying the external perturbations. Our findings showed that depending on different threshold frequencies, electrons change their propagation direction. Besides, the zeros of frequency-dependent imaginary and real parts of the dielectric function corresponding to the Landau undamping and plasmon excitation modes, respectively, have been addressed in the present work. Moreover, we have analyzed the undamped plasmon modes for both intraband and interband transitions. The presence of local perturbations gives the idea to experimentalists that quasi-1D aNRs are proper candidates for the nanoplasmonic applications in infrared rays, visible light, and ultraviolet light regimes of the electromagnetic spectrum with the careful choice of the perturbation.

ACKNOWLEDGMENTS

The author thanks M. Davoudiniya for helpful discussions. This work was partially supported by Iran Science Elites Federation under Grant No. 11/66332.

APPENDIX: PEIERLS PHASE FACTORS

The phase factor $\Delta\Phi_{n,m}$ appearing in $t_{n,m}$ is determined by a line integral of the vector potential $\vec{A}$ through

$$\Delta\Phi_{n,m} = \frac{e}{h}\int_{\vec{R}_n}^{\vec{R}_m} d\vec{l}\cdot\vec{A}, \tag{A1}$$

where e, h, $\vec{R}_1 = (1, 0)a_0$, $\vec{R}_2 = -(1, \sqrt{3})a_0/2$, and $\vec{R}_3 = (-1, \sqrt{3})a_0/2$ with $a_0 = |\vec{R}_{n,m}| = 3.298$ Å are the electron charge, Planck constant, and vectors corresponding to the nearest neighbors, respectively (see Fig. 1). The phase factors for armchair configuration in the Landau gauge $\vec{A} = (0, \mathcal{B}_z x)$ are calculated as

$$\Delta\Phi_{n,m}(\vec{R}_{n,m} = \vec{R}_1) = -a\mathcal{B}_z y_n, \tag{A2a}$$

$$\Delta\Phi_{n,m}(\vec{R}_{n,m} = \vec{R}_2) = -\frac{a_0\mathcal{B}_z}{2}\left[y_n + \frac{\sqrt{3}a_0}{4}\right], \tag{A2b}$$

$$\Delta\Phi_{n,m}(\vec{R}_{n,m} = \vec{R}_3) = +\frac{a_0\mathcal{B}_z}{2}\left[y_n + \frac{\sqrt{3}a_0}{4}\right], \tag{A2c}$$

where y_n is the Si or C atom position in the transverse direction of the ribbon.

[1] C. S. Huang, M. F. Lin, and D. S. Chuu, Solid State Commun. **103**, 603 (1997).
[2] F. L. Shyu and M. F. Lin, Phys. Rev. B **62**, 8508 (2000).
[3] B. Wunsch, T. Stauber, F. Sols, and F. Guinea, New J. Phys. **8**, 318 (2006).
[4] E. H. Hwang and S. Das Sarma, Phys. Rev. B **75**, 205418 (2007).
[5] M. Jablan, H. Buljan, and M. Soljačić, Phys. Rev. B **80**, 245435 (2009).
[6] J. Yan, K. S. Thygesen, and K. W. Jacobsen, Phys. Rev. Lett. **106**, 146803 (2011).
[7] M. Merano, Phys. Rev. A **93**, 013832 (2016).
[8] T. Eberlein, U. Bangert, R. R. Nair, R. Jones, M. Gass, A. L. Bleloch, K. S. Novoselov, A. Geim, and P. R. Briddon, Phys. Rev. B **77**, 233406 (2008).
[9] C. Kramberger, R. Hambach, C. Giorgetti, M. H. Rümmeli, M. Knupfer, J. Fink, B. Büchner, L. Reining, E. Einarsson, S. Maruyama *et al.*, Phys. Rev. Lett. **100**, 196803 (2008).
[10] Y. Liu, R. F. Willis, K. V. Emtsev, and T. Seyller, Phys. Rev. B **78**, 201403(R) (2008).
[11] J. Lu, K. P. Loh, H. Huang, W. Chen, and A. T. S. Wee, Phys. Rev. B **80**, 113410 (2009).
[12] F. H. L. Koppens, D. E. Chang, and F. J. G. de Abajo, Nano Lett. **11**, 3370 (2011).

[13] M. K. Kinyanjui, C. Kramberger, T. Pichler, J. C. Meyer, P. Wachsmuth, G. Benner, and U. Kaiser, Europhys. Lett. **97**, 57005 (2012).

[14] A. N. Grigorenko, M. Polini, and K. S. Novoselov, Nat. Photonics **6**, 749 (2012).

[15] A. Woessner, M. B. Lundeberg, Y. Gao, A. Principi, P. Alonso-González, M. Carrega, K. Watanabe, T. Taniguchi, G. Vignale, M. Polini *et al.*, Nat. Mater. **14**, 421 (2015).

[16] S. C. Liou, C.-S. Shie, C. H. Chen, R. Breitwieser, W. W. Pai, G. Y. Guo, and M.-W. Chu, Phys. Rev. B **91**, 045418 (2015).

[17] S. Maier, *Plasmonics: Fundamentals and Applications* (Springer, New York, 2007).

[18] G. Giuliani and G. Vignale, *Quantum Theory of the Electron Liquid* (Cambridge University Press, Cambridge, England, 2005).

[19] D. K. Gramotnev and S. I. Bozhevolnyi, Nat. Photonics **4**, 83 (2010).

[20] J. A. Schuller, E. S. Barnard, W. Cai, Y. C. Jun, J. S. White, and M. L. Brongersma, Nat. Mater. **9**, 193 (2010).

[21] L. Novotny and N. Van Hulst, Nat. Photonics **5**, 83 (2011).

[22] J. N. Anker, W. P. Hall, O. Lyandres, N. C. Shah, J. Zhao, and R. P. Van Duyne, Nat. Mater. **7**, 442 (2008).

[23] A. Kabashin, P. Evans, S. Pastkovsky, W. Hendren, G. Wurtz, R. Atkinson, R. Pollard, V. Podolskiy, and A. Zayats, Nat. Mater. **8**, 867 (2009).

[24] T. Low, A. Chaves, J. D. Caldwell, A. Kumar, N. X. Fang, P. Avouris, T. F. Heinz, F. Guinea, L. Martin-Moreno, and F. Koppens, Nat. Mater. **16**, 182 (2017).

[25] F. Karimi and I. Knezevic, Phys. Rev. B **96**, 125417 (2017).

[26] V. W. Brar, M. S. Jang, M. Sherrott, J. J. Lopez, and H. A. Atwater, Nano Lett. **13**, 2541 (2013).

[27] T. Low and P. Avouris, ACS Nano **8**, 1086 (2014).

[28] F. J. García de Abajo, ACS Photonics **1**, 135 (2014).

[29] H. Yan, T. Low, W. Zhu, Y. Wu, M. Freitag, X. Li, F. Guinea, P. Avouris, and F. Xia, Nat. Photonics **7**, 394 (2013).

[30] X. Lin, N. Rivera, J. J. López, I. Kaminer, H. Chen, and M. Soljačić, New J. Phys. **18**, 105007 (2016).

[31] X. Lin, Y. Yang, N. Rivera, J. J. López, Y. Shen, I. Kaminer, H. Chen, B. Zhang, J. D. Joannopoulos, and M. Soljaci, Proc. Natl. Acad. Sci. USA **114**, 6717 (2017).

[32] X. Lin, I. Kaminer, X. Shi, F. Gao, Z. Yang, Z. Gao, H. Buljan, J. D. Joannopoulos, M. Soljaci, H. Chen *et al.*, Sci. Adv. **3**, e1601192 (2017).

[33] A. C. Neto, F. Guinea, N. Peres, K. S. Novoselov, and A. K. Geim, Rev. Mod. Phys. **81**, 109 (2009).

[34] L. Ju, B. Geng, J. Horng, C. Girit, M. Martin, Z. Hao, H. A. Bechtel, X. Liang, A. Zettl, Y. R. Shen *et al.*, Nat. Nanotechnol. **6**, 630 (2011).

[35] F. Karimi, A. H. Davoody, and I. Knezevic, Phys. Rev. B **93**, 205421 (2016).

[36] C. A. Downing, E. Mariani, and G. Weick, J. Phys.: Condens. Matter **30**, 025301 (2017).

[37] C. A. Downing and G. Weick, Phys. Rev. B **95**, 125426 (2017).

[38] M. R. Ramezanali, M. M. Vazifeh, R. Asgari, M. Polini, and A. H. MacDonald, J. Phys. A **42**, 214015 (2009).

[39] T. Ando, J. Phys. Soc. Jpn. **75**, 074716 (2006).

[40] N. M. R. Peres, F. Guinea, and A. H. Castro Neto, Phys. Rev. B **73**, 125411 (2006).

[41] V. P. Gusynin, S. G. Sharapov, and J. P. Carbotte, Phys. Rev. Lett. **96**, 256802 (2006).

[42] N. M. R. Peres, T. Stauber, and A. H. C. Neto, Europhys. Lett. **84**, 38002 (2008).

[43] T. Stauber, N. M. R. Peres, and A. H. Castro Neto, Phys. Rev. B **78**, 085418 (2008).

[44] E. H. Hwang and S. Das Sarma, Phys. Rev. B **77**, 195412 (2008).

[45] S. Das Sarma, S. Adam, E. H. Hwang, and E. Rossi, Rev. Mod. Phys. **83**, 407 (2011).

[46] M. Jablan, M. Soljačić, and H. Buljan, Phys. Rev. B **89**, 085415 (2014).

[47] D. Pines, *Elementary Excitations in Solids: Lectures on Protons, Electrons, and Plasmons* (Westview Press, Boulder, CO, 1999), Vol. 5.

[48] J. Y. Wu, S. C. Chen, O. Roslyak, G. Gumbs, and M. F. Lin, ACS Nano **5**, 1026 (2011).

[49] R. D. Mayasari, R. Nuryadi, E. Suharyadi, and K. Abraha, *International Conference on Quality in Research (QiR)* (IEEE, 2015), p. 129.

[50] O. L. Berman, G. Gumbs, and Y. E. Lozovik, Phys. Rev. B **78**, 085401 (2008).

[51] R. Roldan, J.-N. Fuchs, and M. O. Goerbig, Phys. Rev. B **80**, 085408 (2009).

[52] R. Roldan, M. O. Goerbig, and J.-N. Fuchs, Phys. Rev. B **83**, 205406 (2011).

[53] W. J. M. Kort-Kamp, F. S. S. Rosa, F. A. Pinheiro, and C. Farina, Phys. Rev. Lett. **111**, 215504 (2013).

[54] K. Takeda and K. Shiraishi, Phys. Rev. B **50**, 14916 (1994).

[55] S. Cahangirov, M. Topsakal, E. Akturk, H. Şahin, and S. Ciraci, Phys. Rev. Lett. **102**, 236804 (2009).

[56] L.-J. Zhou, Y.-F. Zhang, and L.-M. Wu, Nano Lett. **13**, 5431 (2013).

[57] K. Zhao, M. Zhao, Z. Wang, and Y. Fan, Physica E (Amsterdam) **43**, 440 (2010).

[58] E. Bekaroglu, M. Topsakal, S. Cahangirov, and S. Ciraci, Phys. Rev. B **81**, 075433 (2010).

[59] M. Zhao, Y. Xia, F. Li, R. Q. Zhang, and S.-T. Lee, Phys. Rev. B **71**, 085312 (2005).

[60] Y. Xi, M. Zhao, X. Wang, S. Li, X. He, Z. Wang, and H. Bu, J. Phys. Chem. C **115**, 17743 (2011).

[61] D. Shin, R. Thapa, and N. Park, Curr. Appl. Phys. **15**, 727 (2015).

[62] D. von Deak, D. Singh, E. J. Biddinger, J. C. King, B. Bayram, J. T. Miller, and U. S. Ozkan, J. Catal. **285**, 145 (2012).

[63] J. D. Wiggins-Camacho and K. J. Stevenson, J. Phys. Chem. C **115**, 20002 (2011).

[64] P. Wu, P. Du, H. Zhang, and C. Cai, J. Phys. Chem. C **116**, 20472 (2012).

[65] S. Chen, J. Bi, Y. Zhao, L. Yang, C. Zhang, Y. Ma, Q. Wu, X. Wang, and Z. Hu, Adv. Mater. **24**, 5593 (2012).

[66] H. Jiang, Y. Zhu, Q. Feng, Y. Su, X. Yang, and C. Li, Chem. Eur. J. **20**, 3106 (2014).

[67] C. V. Gomez, M. Pisarra, M. Gravina, and A. Sindona, Beilstein J. Nanotechnol. **8**, 172 (2017).

[68] G. Kiršanské, P. Tighineanu, R. S. Daveau, J. Miguel-Sánchez, P. Lodahl, and S. Stobbe, Phys. Rev. B **94**, 155438 (2016).

[69] M. Berahman, M. Asad, M. Sanaee, and M. H. Sheikhi, Opt. Quant. Electron. **47**, 3289 (2015).

[70] J. Jung and A. H. MacDonald, Phys. Rev. B **87**, 195450 (2013).

[71] H. Zheng, Z. F. Wang, T. Luo, Q. W. Shi, and J. Chen, Phys. Rev. B **75**, 165414 (2007).

[72] G. D. Mahan, *Many Particle Physics* (Plenum, New York, 1993).
[73] A. Brandstetter-Kunc, G. Weick, C. A. Downing, D. Weinmann, and R. A. Jalabert, Phys. Rev. B **94**, 205432 (2016).
[74] J. Khurgin, W.-Y. Tsai, D. P. Tsai, and G. Sun, ACS Photonics **4**, 2871 (2017).
[75] K. Bang, S.-S. Chee, K. Kim, M. Son, H. Jang, B. H. Lee, K. H. Baik, J.-M. Myoung, and M.-H. Ham, Nano Convergence **5**, 7 (2018).
[76] R. Denk *et al.*, Nat. Commun. **5**, 4253 (2014).
[77] B. D. Hoi, M. Yarmohammadi, and M. Davoudiniya, Solid State Commun. **271**, 21 (2018).
[78] K. Wakabayashi, Y. Takane, M. Yamamoto, and M. Sigrist, New J. Phys. **11**, 095016 (2009).
[79] M. Pisarra, A. Sindona, P. Riccardi, V. M. Silkin, and J. M. Pitarke, New J. Phys. **16**, 083003 (2014).
[80] G. Gumbs, A. Balassis, and V. M. Silkin, Phys. Rev. B **96**, 045423 (2017).
[81] B. D. Hoi and M. Yarmohammadi, J. Magn. Magn. Mater **454**, 362 (2018).